Computational Materials Science 46 (2009) 531–544

Contents lists available at ScienceDirect

Computational Materials Science

journal homepage: www.elsevier.com/locate/commatsci

Molecular dynamics study of surface effect on martensitic cubic-to-tetragonal transformation in Ni–Al alloy

Ken-ichi Saitoh [a,b,*,1], Wing Kam Liu [b]

[a] Department of Mechanical Engineering, Kansai University, 3-3-35 Yamate-cho, Suita, Osaka 564-8680, Japan
[b] Department of Mechanical Engineering, Northwestern University, 2145 Sheridan Road, Evanston, IL 60201, USA

ARTICLE INFO

Article history:
Received 6 March 2009
Received in revised form 30 March 2009
Accepted 9 April 2009
Available online 20 May 2009

PACS:
64.60.−i
64.70.K−
61.50.Ah
64.60.Q−

Keywords:
Nickel and aluminum alloy
Molecular dynamics
Martensitic transformation
Stress-induced phase transformation
Finnis–Sinclair potential
Crystalline structure

ABSTRACT

Molecular dynamics (MD) study of martensitic transformation (MT) in nickel and aluminum alloy is performed. The behavior focused on is transformation between crystalline structures from B2 cubic cell to body-centered tetragonal cell, which is simply realized by uniaxial tensile loading. The potential function used is Finnis–Sinclair type having only single energy minimum where B2 structure exists. The availability of this specific many-body potential for stress-induced MT phenomena under uniaxial loading is fully discussed. In MD simulations, martensite phase is induced by tensile stress or strain in the atomic system, as predicted by a potential energy map. It is understood that the characteristic of the potential energy function with regard to deformation is crucial for MT studies and investigating energy-strain or stress–strain map is worthwhile. The MT behavior in the atomic system occurs during a plateau region of stress–strain (S–S) curve of the whole specimen, that is typical for experimental superelastic or shape-memory alloys under uniaxial loading. It is found that, during each MT event, large jump of atomic strain is observed. Owing to single energy minimum, the atomic system shows almost perfect recovery in S–S curve, where the graph comes completely back to initial state after unloaded. Besides, the present paper focuses on surface effect for MT behavior. Since the surface effect is dominant in MT phenomena especially in microscopic specimens, a novel computational scheme for stabilizing condition in which uniaxial loading is always applied together with arbitrary periodic boundary condition(s) is devised. By comparing one-, two-, and three-dimensional models under uniaxial loading, it is recognized that the nucleation behavior depends strongly on the existence of free surface region (including corner edge). When there is no surface, a chaotic nucleation of martensite is observed. On the other hand, the free surface induces first martensite because of less constraint in tensile deformation of unit cells. It is confirmed that the tendency toward MT nucleation corresponds to yield stress or strain of the specimen. In order to define and detect martensite structure as for each atom, an atomic strain measure (ASM) with our own formation is introduced. It is shown that the ASM is very effective to distinguish martensite bct unit structure from others.

© 2009 Elsevier B.V. All rights reserved.

1. Introduction

Martensitic transformation (MT) is recognized as an important mechanism which appears in many engineering functional materials, such as shape memory alloys (SMA), superelastic alloys, strengthened steel, and organic/inorganic polymers. One noteworthy physical nature of MT is its reversible shape change. A good example can be found in materials made of SMA which recover their original shape through heating and cooling. Because of this property, SMAs have been utilized in many engineering fields, such as for surgical purposes and advanced aerospace applications. Experiments have well revealed that this reversibility takes place across all length-scales (sub-μm, μm, mm, cm, m, etc.). Now, we know that it is due to the MT mechanism. The reversibility of these alloys sometimes leads to superelasticity in which the material undergoes extremely large deformations in the elastic regime.

This paper focuses on surface effect in MT. In order for the material to complete MT, nucleation and propagation of new phase are required. It is well known that nucleation in inhomogeneous structure (inhomogeneous nucleation) is easier than that in homogeneous condition. In actual material, many inhomogeneous structures around interface made by precipitates structure, grain

* Corresponding author. Address: Department of Mechanical Engineering, Kansai University, 3-3-35 Yamate-cho, Suita, Osaka 564-8680, Japan. Tel.: +81 6 6368 1111x6371; fax: +81 6 6388 8785.
E-mail address: saitou@ipcku.kansai-u.ac.jp (K. Saitoh).
URL: http://www2.memm.mec.kansai-u.ac.jp/saitoh/nano/index-e.html (K. Saitoh).
[1] Visiting Northwestern University in 2007–2008. Permanent address is Kansai University.

0927-0256/$ - see front matter © 2009 Elsevier B.V. All rights reserved.
doi:10.1016/j.commatsci.2009.04.025

boundary, twin boundary, dislocation, or free surface become a nucleation site. Subsequent propagation of new phase may be affected by these inhomogeneous structures.

The MT mechanism has been investigated extensively by many researchers and there have been a number of attempts to clarify that mechanism. MT is categorized as a non-diffusive, or displacive, phase transformation, in which atomic movement is confined to interatomic lengths. The two stable crystalline phases are called austenite and martensite. That is, during MT, atoms move slightly while keeping their connectivity already established within the crystal unit. This behavior is responsible for complete recovery of shape and it differs from dislocation or slip motion usually found in plastic deformation. In fact, the reversible behavior of the actual materials can be observed visibly. Thus, we can expect an experimentally deduced continuum constitutive law to predict mechanical behavior and want it to be immediately applicable to industrial design [1]. However, the geometrical variety of specimens and the broad range of mechanical conditions in experiment tend to make this deduction quite uncertain. Thus, we should establish our understanding through atomistic theory. Since the essence of MT is atomic-scale movement, some pioneering works [2,3] have pointed out the importance of a theory from atomic-scale.

In this study, therefore, we use molecular dynamics (MD) simulations. The MD simulation is the insightful method to capture atomistic collective behavior in the process of transformation. For Ni–Al systems, a number of potential functions have been proposed so far. Indeed, electronic density calculations based on quantum mechanics are straightforward and very effective. But their performance is poor for the simulation of nonlinear dynamic problem of moving atoms, which is quite crucial for MT phenomena. Accordingly, a classical but semi-empirical approach such as EAM [4] is thought to be optimum.

The thermodynamic theory of Ginzburg and Landau, which is based on transition of free energy, is adopted to the phase field model succeeds in the study of nucleation in MT phenomena [5,6]. However, there exists obscureness between free energy and atomic energy, where the former is directly connected to thermodynamics while the latter is derivable from interatomic potential functions. It seems that the nonlinear dynamic response of atomic systems under mechanical loading or unloading has not been studied in previous frameworks. Nonlinear dynamics of atomic systems is effectively investigated by MD simulations, but, due to computational limitation and technical immaturity, this problems has not been researched extensively [7–14]. Most of MD studies so far applying periodic boundary condition just show a limited aspect of atomic dynamics as for MT. By changing boundary conditions in MD simulation, we will be able to evaluate the surface effect on MT. Even though the researchers sometimes use model with free surface, they did not fully, in the author's knowledge, discuss the surface effect on MT.

In the present paper, we investigate nickel–aluminum (Ni–Al) binary alloys undergoing MT. A recent interesting discovery is that computations predict Ni–Al alloys to be capable of showing recoverable phase transformation in a specimen with nanometer-scale dimensions [9]. The study adopts a wire-shape specimen which has the largest surface ratio and showed clear phase boundaries between martensite and austenite. It is certain that surface plays an important role. Besides, behavior of atoms at four edges of specimen with rectangular cross-section is interesting because they have a coordination number remarkably less than that in flat surface.

According to the phase diagram of Ni–Al binary system, there are some stoichiometric choices: NiAl (B2 or $L1_0$ structure), Ni_3Al ($L1_2$ structure), $NiAl_3$, etc. In the present paper, we focus on structural transformation between B2 (body-centered cubic) and $L1_0$ (face-centered cubic) in Ni–Al alloys, which is similar to the Bain relation between bcc and fcc structures. Clapp et al. referred to this transformation of Ni–Al alloys along with a discussion of potential functions [8,15]. Since a stable phase is actually found at tetragonal bct structure, it should be referred as "cubic-to-tetragonal" phase transformation.

Thus, our objective is to understand atomistic behavior in stress-induced transformation and to discuss about its dependence on free surface (surface effect). For this aim, we propose technically two new methods. First, we introduce a loading/unloading technique for uniaxial tensile tests with variable periodicity in MD simulations. Because of the ambiguous definition of free energy in MD simulations, thermal effects are not considered in the present paper. This is why we focus especially on stress-induced transformation. We show that the surface state altered by periodic conditions enormously changes the results. In the second place, in order to distinguish the crystal phase from the simulated atomic coordinates, we devise an atomic strain measure (ASM). We discuss the implication of ASM and show the general formulation in an expression applicable to MD simulations. To consider atomic-scale value based on continuum notion will be meaningful in connecting the atomistic behavior with the continuum mechanics.

This paper is organized as follows: first, in the following section, we evaluate the ideal energy of crystal structures under homogeneous deformation using an EAM potential utilized here. We display the procedure to treat the MT problem in MD simulations, and show the detailed computational model and its conditions. Then, we show and discuss the results of MD simulation. Finally, we arrive at our conclusion.

2. Theory and method

2.1. Martensite and austenite phases in Ni–Al: definition of martensitic transformation

We start with our definition of crystal phases necessary to detect martensitic transformation (MT) in Ni–Al alloys [16]. Metallurgically, these two phases are specified as martensite and austenite. The crystal structure of Ni–Al systems has been studied metallurgically by using experimental techniques and recently by using theoretical quantum calculations [17]. For Ni-rich compositions, intermediate crystalline structures such as 7 M or 14 M can be found in addition to martensite and austenite [18]. However, stoichiometric compositions used in interatomic potential functions developed for these alloys are normally bound to 50:50 (Ni–Al; B2 or $L1_0$ structure may exist) or 75:25 (Ni_3Al; $L1_2$ structure may exist), because the crystal structure must be defined in smaller units. Inhomogeneous arrangements of atoms typical in defect structures should be considered because they are necessarily included in real materials and may be the first place to trigger phase transformation. Unfortunately, the capability of typical interatomic potentials for alloys does not reach the point where it can directly capture such inhomogeneous situations. Thus, we should begin by capturing the essential features of MT through investigation of relatively regular arrangements along with existing potential function. Especially for MT, it makes good sense to do this because atoms should migrate in a displacive manner, which means the transformation tends to be carried out within the basic crystal cells. For these reasons, we focus on the B2 (austenite) $\rightarrow$ $L1_0$ (martensite) transformation, which is almost identical to the Bain correspondence between bcc and fcc in monoatomic (metallic) systems. This transformation framework in Ni–Al alloy systems makes it easy to analyze microscopic strain in MT, because it only contains uniaxial deformation. In other words, in this study it is assumed that the transformation is not a shear-type but a tensile/compressive-type. This MT mechanism is shown graphically in Fig. 1. By stretching the *c*-axis [0 0 1], the B2 (body-centered) struc-

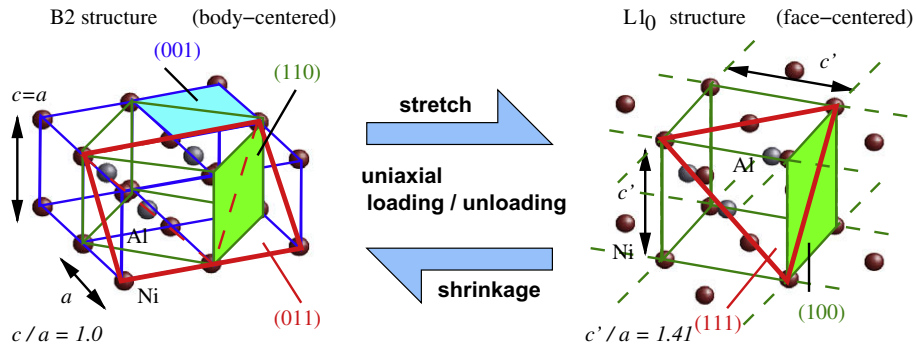

Fig. 1. Crystallography of martensite transformation from B2 structure to $L1_0$ structure in Ni–Al alloy.

ture changes to the $L1_0$ (face-centered) structure. Crystallographically, Miller's index of orientation, $[uvw]_{bc}$, defined in the original body-centered structure (B2) converts into $[uvw]_{fc}$ in the face-centered structure ($L1_0$), using column vectors, as follows:

$$\begin{bmatrix} u \\ v \\ w \end{bmatrix}_{fc} = \frac{1}{2}\begin{pmatrix} 1 & 1 & 0 \\ -1 & 1 & 0 \\ 0 & 0 & 2 \end{pmatrix}\begin{bmatrix} u \\ v \\ w \end{bmatrix}_{bc}, \tag{1}$$

where z-direction is chosen to be the stretching direction. It is important to note that the stretching of the c-axis accompanies shrinkage in the a- and b-axes so that the volume per atom is retained. In other words, generally the B2 $\rightarrow$ $L1_0$ transformation has not only a stretching strain along the c-axis but also a negative strain along the a- and b-axes. In the present paper, the loading direction is prescribed to z hereafter. If the shrinkage in the transverse directions (x, y) are shorter or larger than that expected to complete the Bain relation, the unit structures stays at bct (body-centered tetragonal) or shifts toward fct (face-centered tetragonal). Even in these cases, the driving force for MT is always found uniaxially along the stretched c-axis. Therefore, our MD simulation boundary condition for MT is required to realize this uniaxial condition, which we discuss in later sections.

2.2. Potential functions for Ni–Al and their characteristics in homogeneous deformation

There exist several potential functions for Ni–Al systems. For example, they can be found in literature those proposed by Voter and Chen [19], Yan et al. [20], Foiles and Daw [21], Rubini and Ballone [22], Farkas et al. [23,24], Ludwig and Gumbsch [25], and Ozgen and Adiguzel [11]. However, there still exists room for further development to include first-principle quantum calculations. At present, we assume that the EAM (embedded atom method) [4] is a suitable framework of potential function for MD analysis. This is because time-evolving many-body dynamics simulations provide with insightful information of collective motions in atomic system. Also, even though the thermal (kinetic) effect is not mentioned in this paper, a simulation at finite temperature is essential. By using strict quantum calculation, activation energy of MT behavior can be captured by seeking the most probable route, but this is not adequate enough to recognize the transformation behavior because there may exist multiple routes of transformation due to the many-body nature, collective motion or kinetic effect.

The total energy of an atomic system expressed by the EAM is

$$E = \sum_i \left\{ F_i(\rho_i) + \frac{1}{2}\sum_j \phi_{ij}(r_{ij}) \right\}, \tag{2}$$

where r_{ij} is the distance between atoms i and j, $F_i(\rho_i)$ is the embedded function of electron density, ρ_i, which is defined at the site of the i atom. We adopt one of the EAM potential functions shown above. The potential we use is that proposed by Yan et al. [20] which is constructed by proper fitting to crystal energy of B2 structure and its mechanical properties. It is formulated along with the embedding function of the Finnis–Sinclair type [26], which is expressed by the square root of the electron density at the site of interest. Table 1 shows the basic properties of the B2 structure which are reproduced by this potential. The reader can refer to original literature for further information of formulation and availability of this potential [20].

For this potential, the authors [20] mentioned that the energetic minimum can be found for the B2 structure but not for the $L1_0$ structure. However, it should be noted that their results are limited by constant volume, so we seek energy variation with an optimum shrinkage along a- and b-axes (a- and b-axes are equivalent in this case). An energy-deformation map obtained for this potential is displayed and compared in Fig. 2.

As mentioned above, stretching along the c-axis (see positive domain in ε_1: vertical axis of the graph) results in shrinkage along the a- and b-axes (see negative domain in ε_2: horizontal axis of the graphs). In Fig. 2, the energy minimum curve, which is obtained by optimizing the a- and b-axes to give the lowest energy for the prescribed c-axis length, is shown by the dot-and-broken line, connecting points as $A \rightarrow B \rightarrow C \rightarrow D$ and $A \rightarrow E$. This EAM potential shows only a single minimum exactly at point $A : (\varepsilon_1, \varepsilon_2) = (0, 0)$.

The volume-conserving deformation route shown by the broken line in Fig. 2 deviates from the energy minimum curve, which means that the crystal energy during deformation with conserved volume does not guarantee minimum energy. In a static sense, i.e. without thermal fluctuation, we expect that the structure changes along the path of minimized energy. Fig. 3 shows the energy change along the energy minimum curve of Fig. 2. The EAM potential we use shows only one well at the B2 structure and, at the same time, it shows some degradation in gradient around $c/a = 1.3$. Müller [27] pointed out that, by

Table 1
Properties for B2 structure reproduced by interatomic potential by Yan et al. [20].

Property	Property	Unit	EAM [20]	Experiment [20]
Lattice constant	a_0	nm	0.288	0.2887
Cohesive energy	E_c	eV	4.52	4.52–4.77
Elastic constant	C_{11}	10^{11} Pa	2.115	2.115
Elastic constant	C_{12}	10^{11} Pa	1.426	1.426
Elastic constant	C_{44}	10^{11} Pa	1.138	1.122
Inverse of compliance	$1/S_{11}$	10^{11} Pa	0.9662	–
Cutoff length	r_c	nm	0.496	–

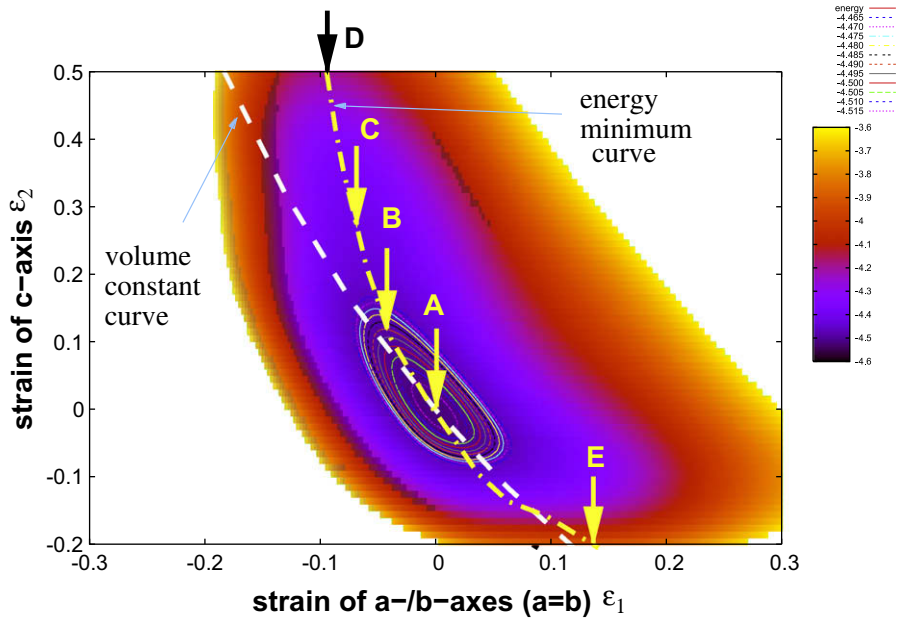

Fig. 2. Energy change in which lattice lengths c and $a(=b)$ vary independently (energy-deformation map) using the EAM (FS-type) potential.

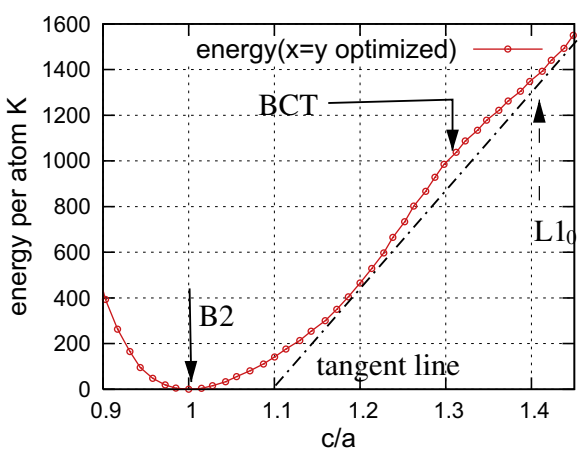

Fig. 3. Energy minimum path along c-axis stretch with optimized transverse strain. Note that horizontal value is ratio c/a.

using a common tangent to the convex parts in a free energy curve like Fig. 3, the loaded body prefers the tangent value. This is because for a given stretch (i.e. fixing at a certain c/a in Fig. 3) the tangent provides a lower energy than the curve itself. This leads to the possibility that this EAM potential in a loaded state exhibits martensite structure at the point denoted by "BCT" in Fig. 3.

Next, we discuss the relation between force (stress) and structure. The mechanical response of the atomic system under MT is well represented by the stress–strain relation estimated by the interatomic potential function. In an atomic system, due to its discrete nature, complete accordance with continuum stress (Cauchy stress) is difficult, but atomic stress can be used successfully so far. By averaging atomic stress over the whole system and, if needed, over the time line, we will get satisfactory estimation comparable with continuum stress, though some approximations are necessary. In the present study, the atomic stress tensor of individual atoms is calculated using effective pairwise approximation of the EAM [28] as follows:

$$\sigma^{\alpha\beta} = \frac{1}{N}\sum_{i=1}^{N}\left[\frac{1}{2\Omega_i}\sum_{j\in neighbor}\frac{\partial\phi_{\mathrm{eff}}(r)}{\partial r}\bigg|_{r=r_{ij}}\frac{r_{ij}^{\alpha}r_{ij}^{\beta}}{r_{ij}}\right], \tag{3}$$

where $\phi_{\mathrm{eff}}(r)$ is the effective pairwise potential formulated from Eq. (2), r_{ij}^{α} is the difference vector between atoms i and j, Ω_i is an atomic volume allocated to atom i, and N is the total number of atoms in the system. Greek indices $(\alpha, \beta, \ldots = 1, 2, 3)$ denote Cartesian components. The normal components of the stress tensor are denoted by $\sigma^{11}, \sigma^{22}, \sigma^{33}$ or $\sigma_x, \sigma_y, \sigma_z$. Since the atomic volume changes in the course of deformation, the value of Ω_i should be modified, but we use a constant value for atomic stress calculation. This changes the absolute value of atomic stress, but does not affect the zero-stress (balanced) condition.

Fig. 4 shows the stress-deformation map of the crystal under the same homogeneous deformation as used in Fig. 2, where a normal stress component in the stretching direction (σ_z) is shown. The bundle of contour lines divides the whole area into positive σ_z and negative σ_z. That is, these bundles almost correspond to the zero-stress ($\sigma_z = 0$) curve. The volume-conserving curve and the minimum energy curve are shown in the figure as well. Obviously, all of the lines intersect at the origin $(\varepsilon_1, \varepsilon_2) = (0, 0)$. Note that the zero-stress curves for σ_z do not match with the minimum energy curve, because σ_z presents the energy gradient only in the particular direction. In the deformed state, it makes sense that not all of the components of stress vanish. Fig. 5 shows normal stress components σ_x, σ_y and σ_z obtained along the energy minimum curve. It is verified that only the tensile component, σ_z, varies whereas components in other directions vanish. That is, the energy minimum curve completely coincides with the zero-stress of transverse stress, σ_x, σ_y. In these figures, the atomic volume modified along with stretching of the crystal is compared with that not modified. The local maximum point $(\sigma_z, \varepsilon_z)$ is (4.7 GPa, 0.17) for this EAM potential, where ε_z is calculated by $c/c_0 - 1$, and c_0 is the original length of the c-axis. Moreover, local minimum point $(\sigma_z, \varepsilon_z)$ is (2.8 GPa, 0.28). The notion of crystalline stability in the case of stretch in the [001] direction of a cubic crystal was reviewed by Milstein [29] and is helpful. In Milstein's discussion, the first and third zero-stress denote stable crystal phases. As explained by Fig. 5b, it is easily understood that the graph with three-zero features naturally satisfies the condition of multiple stable structures.

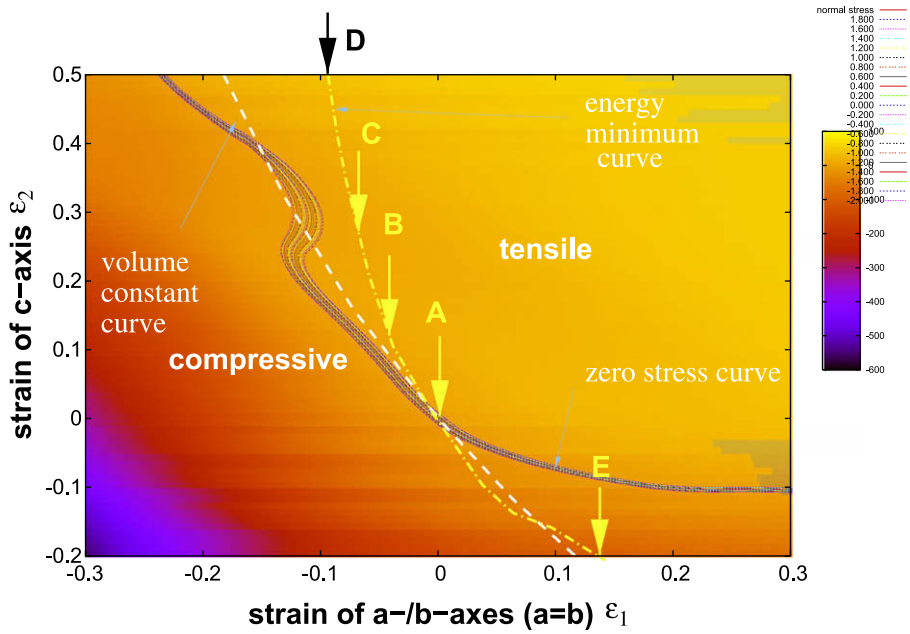

Fig. 4. Change of stress σ_z in which lattice lengths c and $a(=b)$ vary independently (stress-deformation map).

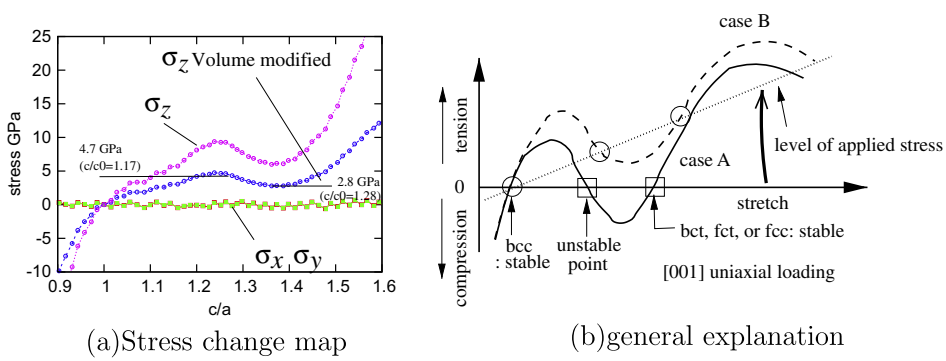

Fig. 5. Stress minimum path along c-axis change. Horizontal and vertical axes are c/a and σ_z, respectively. After Milstein [29], (b) explains the meaning of zero-stress points (case A: solid curve). Even if a stress-stretch relation shows only one zero-stress, applied stress exerted from outside can pull up the balance line to make multiple critical points (case B: broken curve and dotted line).

This idea can be expanded to the graph with the one-zero case (exactly this potential's case: Fig. 5a). A certain applied stress exerted from outside (e.g. by strain constraint) pulls the balance line up so as to intersect with the one-zero graph at multiple points. Physically, this means that a certain amount of stress is required to maintain the alternative structure (martensite) in using this EAM potential.

2.3. Analyzing deformation using atomic strain measure

Martensitic transformation (MT) is categorized into the group of displacive transformation, which is with small displacement of atoms. Therefore, the deformation under MT is captured inside the basic crystal unit as shown in Section 2.1. In SMA alloys, either the microscopic twinning–detwinning mechanism or the Bain-type transformation from bcc to fcc is thought to be owing to MT. Basically the transformation should be free from topological change of atomic connectivity.

In order to comprehend the deformation under MT, it is useful to introduce a strain measure at the atomic scale. As can be found in ordinary solid mechanics textbooks, strain is a continuum notion and is defined by infinitesimal segments between material points. This conceptual fact makes it involved to define a strain measure in atomic system. However, if a homogeneous deformation field can be assumed, this value has the same physical meaning as the continuum strain. For example, the reader can refer to earlier work done by Mott et al. [30] and Buehler et al. [31] Thus, our purpose here is to seek a formulation of atomic strain measure (ASM) suitable for MD simulations of MT behavior. The ASM proposed by us is described below. The continuum definition of Green's strain measure tensor $\varepsilon^{\alpha\beta}$ is a prototype. In a continuum description of a body, the difference in the squared length of a the line segment measured before and after deformation is given by

$$dx^\alpha dx^\alpha - dX^\alpha dX^\alpha = 2dX^\alpha \varepsilon^{\alpha\beta} dX^\beta, \tag{4}$$

where α and β indicate components ($\alpha, \beta = 1, 2, 3$) with the summation convention applied. X^α and x^α are reference and current position vectors, respectively. The d in front of X or x indicates an infinitesimal value. When the deformation is small enough, the strain tensor in a continuum body is given by

$$\varepsilon^{\alpha\beta} = \frac{1}{2}\left(\frac{\partial u^\alpha}{\partial X^\beta} + \frac{\partial u^\beta}{\partial X^\alpha}\right), \tag{5}$$

where $u^\alpha = u^\alpha(\boldsymbol{X})$ is the displacement evaluated at the undeformed point $\boldsymbol{X} = (X^1, X^2, X^3)$.

We derive a definition of atomic strain measure for an atomic system, referring to Eq. (5). Instead of using infinitesimal segments, strain measure of atomic system can be defined for interatomic segments denoted by vector between atoms i and j,

$$r_{ij}^\alpha = r_j^\alpha - r_i^\alpha. \tag{6}$$

As explained in Fig. 6, following the continuum expression Eq. (4), the difference in the interatomic distance between atoms i and j measured before and after deformation is expressed by,

$$r_{ij}^\alpha r_{ij}^\alpha - r_{ij}^\alpha(0) r_{ij}^\alpha(0) = 2 r_{ij}^\alpha(0) \varepsilon_{ij}^{\alpha\beta} r_{ij}^\beta(0), \tag{7}$$

where variables with "(0)" are those of the original (undeformed) value, which conceptually correspond to the $\boldsymbol{X}$ variables in a continuum definition. If the deformation gradient field $F^{\alpha\beta}$ can be defined, it should be,

$$F^{\alpha\beta} = \frac{\partial r_{ij}^\alpha}{\partial r_{ij}^\beta(0)}. \tag{8}$$

Then, the strain measure given by Eq. (7) becomes

$$\varepsilon_{ij}^{\alpha\beta} = \frac{1}{2}\left(F^{\gamma\alpha} F^{\gamma\beta} - \delta^{\alpha\beta}\right), \tag{9}$$

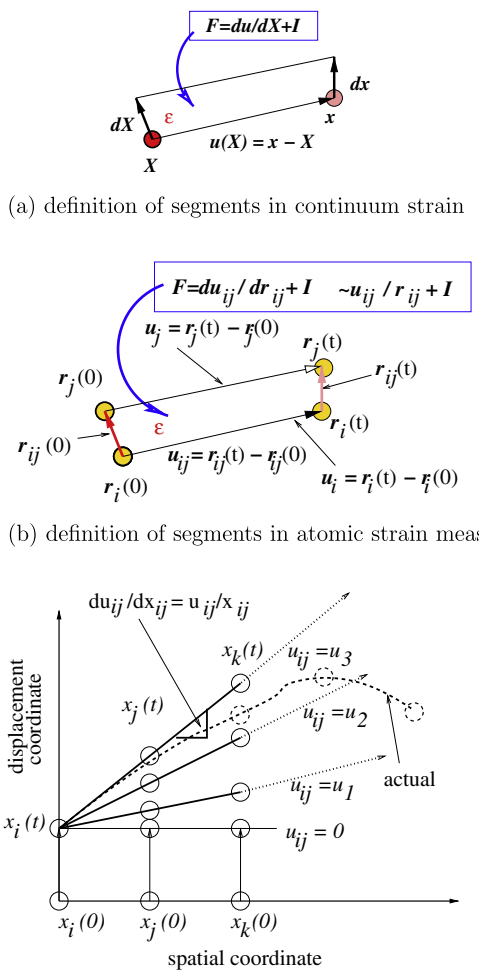

(a) definition of segments in continuum strain

(b) definition of segments in atomic strain measure

(c) assumption of homogeneous (uniform in space) deformation

Fig. 6. Concepts of atomic strain measure (ASM); definition of variables and explanation of assumption.

where $\delta^{\alpha\beta}$ is Kronecker's delta notation. We introduce the displacement of the line segment u_{ij}^α,

$$\begin{aligned} u_{ij}^\alpha &= r_{ij}^\alpha - r_{ij}^\alpha(0) = (r_j^\alpha - r_i^\alpha) - (r_j^\alpha(0) - r_i^\alpha(0)) \\ &= (r_j^\alpha - r_j^\alpha(0)) - (r_i^\alpha - r_i^\alpha(0)), \end{aligned} \tag{10}$$

which is calculated by individual atomic time-evolution. Using the relation, Eq. (10), for the deformation gradient, Eq. (8), the detailed form of Eq. (9) becomes as follows:

$$\begin{aligned} \varepsilon_{ij}^{\alpha\beta} &= \frac{1}{2}\left(\frac{\partial u_{ij}^\alpha}{\partial r_{ij}^\beta(0)} + \frac{\partial u_{ij}^\beta}{\partial r_{ij}^\alpha(0)} + \frac{\partial u_{ij}^\gamma}{\partial r_{ij}^\alpha(0)} \frac{\partial u_{ij}^\gamma}{\partial r_{ij}^\beta(0)}\right) \\ &\approx \frac{1}{2}\left(\frac{\partial u_{ij}^\alpha}{\partial r_{ij}^\beta(0)} + \frac{\partial u_{ij}^\beta}{\partial r_{ij}^\alpha(0)}\right). \end{aligned} \tag{11}$$

The last equation is justified for small deformations.

The expression (11) is ideal for defining the strain concerning the line segment r_{ij}^α but is not useful for computation, because the denominators are just a component of the interatomic vector which can be zero. By postulating some assumptions for Eq. (11), we avoid the divergent nature. First, we assume that the displacement field of a segment r_{ij}^α depends primarily on interatomic length r_{ij}. Assuming that it depends on the initial value $r_{ij}(0)$, the derivative in Eq. (11) is given by

$$\frac{\partial u_{ij}^\alpha}{\partial r_{ij}^\beta(0)} \approx \frac{\partial u_{ij}^\alpha}{\partial r_{ij}(0)} \frac{\partial r_{ij}(0)}{\partial r_{ij}^\beta(0)} = \frac{\partial u_{ij}^\alpha}{\partial r_{ij}(0)} \frac{r_{ij}^\beta(0)}{r_{ij}(0)}. \tag{12}$$

In addition, as explained in Fig. 6c, we assume that the displacement u_{ij}^α and interatomic displacement $r_{ij}(0)$ have a linear relation, that is, $\partial u_{ij}^\alpha / \partial r_{ij}(0) \approx u_{ij}^\alpha / r_{ij}(0)$. Then, the derivative is given by

$$\frac{\partial u_{ij}^\alpha}{\partial r_{ij}^\beta(0)} \approx \frac{u_{ij}^\alpha}{r_{ij}(0)} \frac{r_{ij}^\beta(0)}{r_{ij}(0)}. \tag{13}$$

The dependence of strain on interatomic distance $r_{ij}(0)$ is reasonable because the contribution from relatively nearby atoms should be dominant. The contributions are smaller for the distant atoms. A linear relation between displacement and distance is a strong assumption which is correctly supported only for homogeneous deformation. The final form of atomic strain measure for the interatomic segment r_{ij}^α is given by

$$\varepsilon_{ij}^{\alpha\beta} = \frac{1}{2(r_{ij}(0))^2}\left[u_{ij}^\alpha r_{ij}^\beta(0) + u_{ij}^\beta r_{ij}^\alpha(0)\right]. \tag{14}$$

In Eq. (14), all of the components except for u_{ij}^α or u_{ij}^β, have been calculated from the reference (undeformed) atomic configuration, $r_i^\alpha(0)$. The displacements, u_{ij}^α and u_{ij}^β, must be calculated from the current atomic positions.

In order to evaluate strain at individual atomic sites, Eq. (14) is simply averaged over the neighboring atoms which the atom i interacts with, as follows:

$$\varepsilon_i^{\alpha\beta} = \frac{1}{N_{neighbor}} \sum_{j=1}^{N_{neighbor}} \varepsilon_{ij}^{\alpha\beta}, \tag{15}$$

where $N_{neighbor}$ is the number of neighbors. This is how the "atomic strain measure (ASM)" of atom i is defined. In this formulation, even if the displacement between distant neighbors is larger, the ASM is always scaled by the distance, $r_{ij}(0)$. If we need to examine the strain in the very vicinity of an atom, we may confine interaction to a certain cutoff distance. This expression is effective for estimating lattice distortion which occurs during MT.

Despite the deficiency due to the simple assumptions of homogeneous deformation and linear relation between displacement and distance, the merit is generous instead. In order to check if an adequate evaluation of strain is possible, we calculate ASM val-

ues using Eq. (15) for the ideal crystal structure of B2. Under periodic condition, uniaxial and homogeneous stretching along the *c*-axis (*z*-direction) is applied. The contraction in the transverse direction (*x*- or *y*-direction) is estimated by the volume-conserving condition. Table 2 shows the correspondence between the applied strain and the calculated atomic strain measure. Since the lattice constant of the reference structure is $a_0 = 0.2887$ nm, the cutoff length of 0.3000 nm is chosen in order to include up to second neighbors. An almost linear relation between the applied strain, ε_z, and the estimated atomic strain measure, ε_i^{33} is obtained. Indeed, $\varepsilon_i^{\alpha\beta}$ defined by Eq. (15) involves contribution from atoms located in the inclined direction and those atoms tend to reduce the calculated value. But, referring to the relation in Table 2, the volume ratio calculated by $(1+\varepsilon_i^{11})(1+\varepsilon_i^{22})(1+\varepsilon_i^{33})$ results in almost unity with small error. That is, the volume-conserving condition is also true for the ASM components in this case.

From the Bain relation or the relation between energy and deformation described in Section 2.2, martensite structure of Ni–Al alloy will appear in the range, $1 < c/a < \sqrt{2} = 1.41$. In this range the ASM shows a remarkably small error less than 0.01%. In our MD calculation, by using an ASM component ε_i^{33} together with a criterion ε_{cr}^{33}, we can detect the martensite phase in atom-by-atom basis. It is assumed that $\varepsilon_{cr}^{33} = 0.06$–$0.10$ (6–10%), which corresponds to $c/c_0 = 1.08$–1.30. It is important to note that the ASM does not quantitatively provide exact value of strain but rather qualitatively shows difference between crystalline states. Roughly speaking, the actual strain is three times larger than the ASM values.

2.4. Uniaxial straining of molecular dynamics cell with varying surface effect

In order to carry out martensitic transformation in the Ni–Al system, uniaxial loading along the *c*-axis is required for the MD simulation box (MD simulation cell). At the same time, by applying free surface conditions in the transverse directions, it is possible to model a very narrow nanowire structure. As experimental facts, the interface between the parent crystal and the hard inclusion, free surfaces or grain boundaries provides with trigger sites for nucleation of transformation in the alloys. In other words, inhomogeneity in the structure is important for nucleation of transformation. However, the nanowire-shape is presumed to be with too much outcome of transformation as revealed in the literature [9]. At this point, it is necessary to introduce a boundary condition by which the surface effect is controllable. The leftmost picture in Fig. 7a shows an ordinary boundary condition for tensile loading of the MD cell. In order to maintain periodicity in transverse directions (*x*, *y*, or both), it is necessary to place imaginary and periodic cells in these directions (this is just referring to usual periodic boundary condition). However, since at the same time the stretched crystal strives to perform Poisson's contraction, predetermined cell lengths in periodic directions will cause additional residual stress in the cell. This problem seems to have been resolved by well-known MD technique with constant-pressure ensemble (NPT) or the constant-stress ensemble (N**S**T). However, these methods often result in no ignorable oscillation of the cell length due to immediate response to imbalance in stress component. This unrealistic behavior will spoil MT analysis in the MD simulation.

The remedy suitable for our present purpose is as follows:

1. In the loading direction, the cell length steadily increases with the prescribed strain rate $\dot{\epsilon}^I$ (i.e. strain increases by $\Delta\epsilon^{\alpha\beta} = \dot{\epsilon}^I \Delta t$ during a time increment Δt. The superscript "$\alpha\beta$" implies the loading direction). At the same time, the atomic coordinates are subject to strain corresponding to cell length.
2. In directions other than the loading direction, the cell length is modified with another prescribed strain rate $\dot{\epsilon}^{II}$ so as to reduce difference between current stress and targeted one.

When the targeted and current stresses are $\sigma_0^{\alpha\beta}$ and $\sigma^{\alpha\beta}$ respectively, the change in strain during each time increment Δt is given by

$$\Delta\epsilon^{\alpha\beta} = \begin{cases} -\mathrm{sgn}(\sigma^{\alpha\beta} - \sigma_0^{\alpha\beta})\ \dot{\epsilon}^{II}\Delta t & (|\sigma^{\alpha\beta} - \sigma_0^{\alpha\beta}| > \eta) \\ 0 & (|\sigma^{\alpha\beta} - \sigma_0^{\alpha\beta}| \leqslant \eta) \end{cases} \tag{16}$$

(a component "$\alpha\beta$" implies non-loading direction) where η is a certain criterion by which the stress component can be recognized as almost equal to the targeted value.

The former action 1 means control of strain in the loading direction, whereas the latter action 2 means structural relaxation in the other directions. The latter action 2 may be called the "stabilizing condition". The increment of strain tensor $\Delta\epsilon^{\alpha\beta}$ is applied to both atomic coordinates $r_i^\alpha (i = 1 \sim N)$ and cell length l^α, so that

$$\begin{aligned} r_i^{\alpha*} &= (\delta^{\alpha\beta} + \Delta\epsilon^{\alpha\beta}) r_i^\beta \\ l^{\alpha*} &= (\delta^{\alpha\beta} + \Delta\epsilon^{\alpha\beta}) l^\beta, \end{aligned} \tag{17}$$

where variables with an asterisk are the modified value. In the present study, shear deformation is not considered and off-diagonal components in the strain tensor $\Delta\epsilon^{\alpha\beta}$ are omitted as zero. We are going to show the general case including shear deformation in further study. These procedures are explained schematically in Fig. 7b. By using a finite strain rate $\dot{\epsilon}^{II}$ as well as $\dot{\epsilon}^I$, atoms in the simulation box are allowed to equilibrate with gradually varying strain at each stage. Meanwhile, the system obtains the targeted stress value. By using this technique, even when the specimen is in a high stress state, it is possible to bring the system to any specified stress state, $\sigma_0^{\alpha\beta}$. This also enables unloading simulation which starts from a certain loaded state. Table 3 shows the relation between boundary

Table 2
Relation between atomic strain measure proposed here and applied strain; Homogeneous strain is applied to ideal and periodic structure. The reference crystal is B2 structure. It is stretched along the *c*-axis (in $z(=33)$ direction) with the volume held constant. The lattice constant in B2 is 0.2887 nm and the cutoff distance is 0.30 nm. The volumetric error can be calculated by using $V/V_0 = (1+\varepsilon_i^{11})^2(1+\varepsilon_i^{33})$. c_0 is the initial length of *c*-axis. A stretched bct structure may be also regarded as a compressed fct structure.

Stretch		Atomic strain measure		Volume error	cf. Corresponding structure
c/c_0	c/a	ε_i^{11}	ε_i^{33}	$V/V_0 - 1$	
0.95	0.93	0.008	−0.017	0.000	bct (Compressed)
0.99	0.99	0.002	−0.003	0.000	bct (Compressed)
1.00	1.00	0.000	0.000	0.000	B2:bcc
1.01	1.02	−0.002	0.003	0.000	bct (Stretched)
1.05	1.08	−0.008	0.017	0.000	bct (Stretched)
1.10	1.15	−0.016	0.033	0.001	bct (Stretched)
1.20	1.31	−0.029	0.067	0.006	bct (Stretched)
1.26	1.41	−0.036	0.087	0.009	$L1_0$:fcc
1.30	1.48	−0.041	0.100	0.012	fct (Stretched)

conditions and mechanical processes. Whatever periodicity the model has, uniaxial loading is achieved by using the new "stabilizing" condition together with the loading condition. The one-dimensional (1D), two-dimensional (2D), and three-dimensional (3D) periodic uniaxial boundary conditions are possible as shown in Fig. 7a.

2.5. Molecular dynamics model of Ni–Al alloy with uniaxial deformation

The computation model of Ni–Al alloy for MD simulation is shown in Fig. 8. Conditions of calculation are shown in Table 4. In the direction of tensile loading (*z*-direction), the periodic condition is always applied to the specimen. In order to assess the surface effect on MT, three models are considered which have different conditions in the two directions other than the tensile direction. The detail of the models are listed in Table 4. At the free surfaces, the model is always terminated with nickel atoms, so the composition of nickel is larger than that of aluminum except in the case of the 3D periodic model. All structures start from the B2 austenite phase, where the tensile direction coincides with the $[001]_{bc}$ crystalline orientation. This is because the crystal is expected to produce tetragonal (bct) structure from B2 structure by stretching in the orientation shown in Fig. 1.

Temperature control which utilizes the velocity scaling scheme is applied to the model at all times, where atomic velocities are slowed down so that the system temperature does not exceed 10 K. The reason why the temperature of the system is kept at such a low constant is that, while we do not fully discuss thermally induced MT, we need some thermal fluctuation for dynamics. Before loading, the structure is equilibrated by using the "stabilizing" technique described in the previous section. "Stabilizing" is per-

Table 3
Relation between boundary conditions and mechanical processes; *x*- and *y*-directions are equivalent and exchangeable. As mentioned in the text, the new "stabilizing condition" is shown. "Periodic" refers to the standard periodic boundary condition. "Free" means that there are free surfaces in that direction. Reversing the direction of tensile loading would realize compressive loading.

Boundary condition			Periodical dimension	Mechanical process
x	*y*	*z*		
Periodic	Periodic	Periodic	3D	*NVT* or *NVE* Ensemble
Stabilizing	Stabilizing	Loading	3D	Uniaxial loading
Stabilizing	Stabilizing	Stabilizing	3D	Relaxation or unloading
Free	Stabilizing	Loading	2D	Uniaxial loading
Free	Stabilizing	Stabilizing	2D	Relaxation or unloading
Free	Free	Loading	1D	Uniaxial loading
Free	Free	Stabilizing	1D	Relaxation or unloading

* "Loading" could be either tensile or compressive.

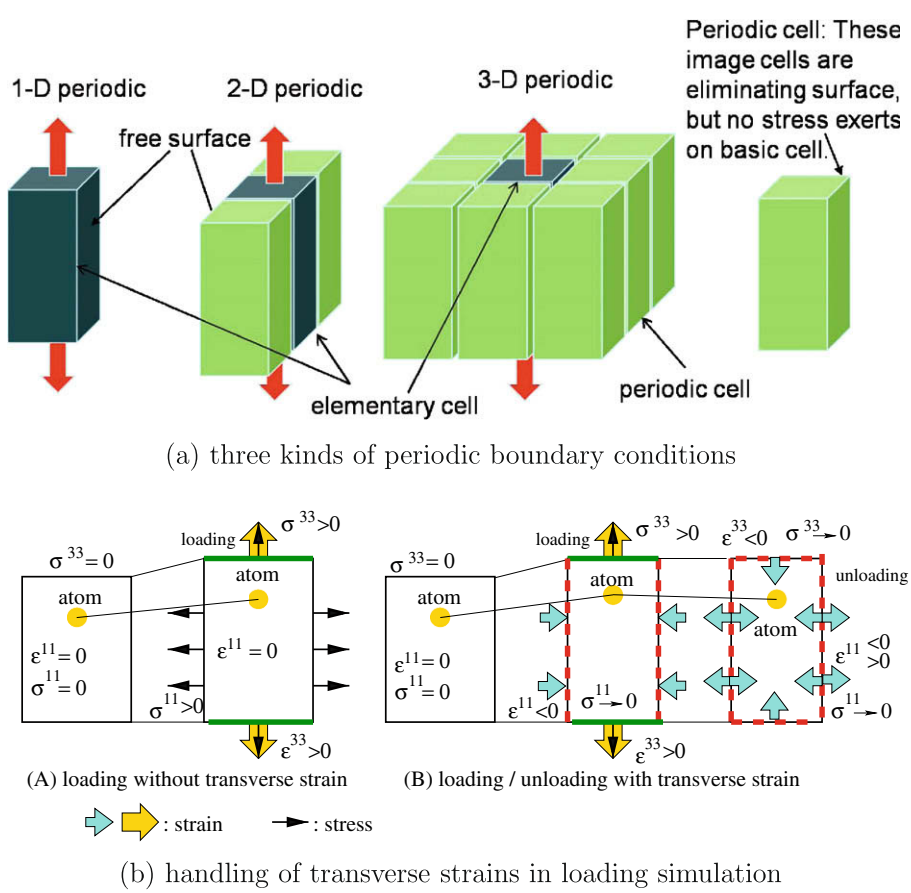

Fig. 7. Uniaxial loading condition with controllable periodicity of unit cell.

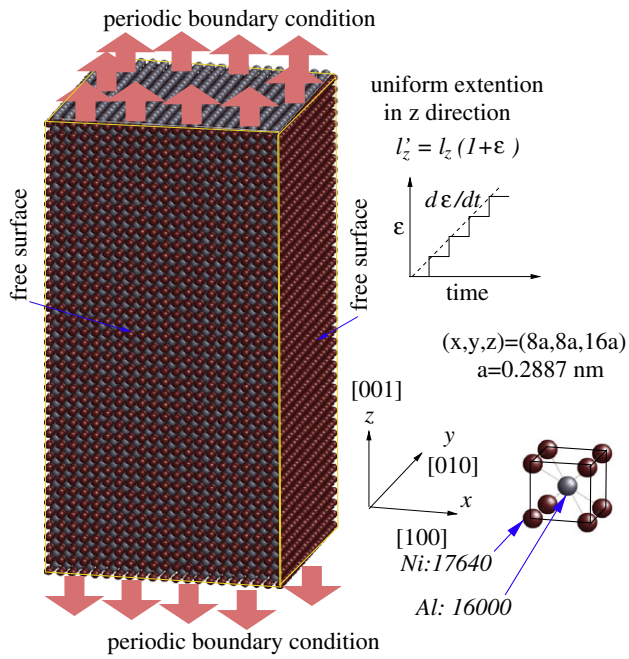

Fig. 8. MD computation model.

Table 4
Calculation conditions.

Property	Unit	Value(s)		
		1D Model	2D Model	3D Model
The number of atoms		33,640	32,800	32,000
The number of Ni atoms		17,640	16,800	16,000
The number of Al atoms			16,000	
Elementary cell size ($x \times y \times z$)	nm		$5.774 \times 5.774 \times 1.1548$	
Initial lattice constant a_0	nm		0.2887	
Controlling temperature	K		10.0	
Strain rate $\dot{\epsilon}^I$ (to stretch)	10^9 1/s		3.0 (in z direction)	
Strain rate $\dot{\epsilon}^{II}$ (to control stress)	10^9 1/s		0.1–10.0 (2D: in y-direction, 3D: in x- and y-directions)	
Numerical integration scheme			4-Value Gear method	
Time increment	fs		2.0	

formed with the condition in which targeted stresses of $\sigma_x, \sigma_y, \sigma_z$ are all zero. The standard strain rate for tensile loading is $\dot{\epsilon}^I = 3.0 \times 10^9$ 1/s. Other values, 1.0×10^{10} 1/s (fast case) or 1.0×10^9 1/s (slow case) have been checked, but the change in behavior is negligible.

First, tensile loading in the z-direction is applied. Then, the loading is stopped at an arbitrary point where the specimen has not yet broken but has sufficiently transformed. The point of this stoppage is found in the computed stress–strain curve of the whole specimen. After that, the specimen is unloaded under the stabilizing condition until the stress component in the loading direction σ_z becomes zero.

3. Results and discussion

3.1. Stress change in loading and unloading of one-dimensional periodic case: check of reversibility

Stress components $\sigma^{11}(=\sigma_x), \sigma^{22}(=\sigma_y), \sigma^{33}(=\sigma_z), \sigma^{12}, \sigma^{23}, \sigma^{31}$ averaged over the whole atomic system are plotted with regard to the total strain in the loading direction $\varepsilon^{33}(=\varepsilon_z)$ of the specimen, as shown in Fig. 9. That is, this is the uniaxial stress–strain curve (S–S curve) of the specimen. Fig. 9 shows the graph for the 1D periodic case. Strain ε_z is estimated by the relation, $\varepsilon_z = (l_z - l_z(0))/l_z(0)$, where l_z and $l_z(0)$ are current and undeformed cell lengths in the loading direction, respectively. Only σ_z varies with strain, which means that the present boundary condition for uniaxial loading works very well. The component σ_z increases with strain showing a linear elastic response. However, before yielding takes place at point B in the graph, there exists some degradation of the gradient near point A. The broken lines denoted by S1 and S2 are guides for the gradients. Line S2 reveals that the gradient is about 47 GPa. This is smaller than the inverse value of a compliance calculated by, $1/S_{11} = (C_{11} - C_{12})(C_{11} + 2C_{12})/(C_{11} + C_{12}) = 96.62$ GPa, as in Table 1. However, line S1, which is fit to the curve at the very beginning of loading, shows that the gradient is about 100 GPa, which agrees well with the theoretical value of $1/S_{11}$. Basically, elastic constant of the atomic system originates from the curvature of the present interatomic potential function at equilibrium interatomic spacing, that is, for very small strain. Therefore, it is understood that the decrease of the overall gradient represented by S2 is due to non-linearity of the potential function and is reasonable.

Further straining after yielding produces a plateau region from point B to point D in Fig. 9, where an approximately constant stress is applied to the specimen during deformation. Interestingly, despite the stress level being quite different, the total shape of the computed S–S curve resembles those obtained by experiment on macro-sized specimens [32]. Experiments reveal that the specimen undergoes MT within this plateau region. At point E, the specimen begins to break. The stress and strain relation from D to E is almost linear, which means the crystal behaves in elastic manner again. The gradient $(1/S_{11})$ of line S3 is 113 GPa, which is larger than those found in the earlier stages. It is understood that the first $(O \rightarrow B)$ and the second $(D \rightarrow E)$ linear responses correspond to the elastic response of complete austenite and martensite structures, respectively. Since the strain $\varepsilon_z = 0.35$ is large enough to create martensite units (bct) which has already been specified in Section 2.2 and Fig. 3, the final linear response is identified as for a martensite phase. This leads to the fact that MT emerges between these two elastic regions. In order to see whether the strain, stress, and structure are reversible or not, tensile loading is stopped during the final elastic response. Fig. 10 shows the stress–strain $(\sigma_z - \varepsilon_z)$ curves which include the curve of unloading as well as

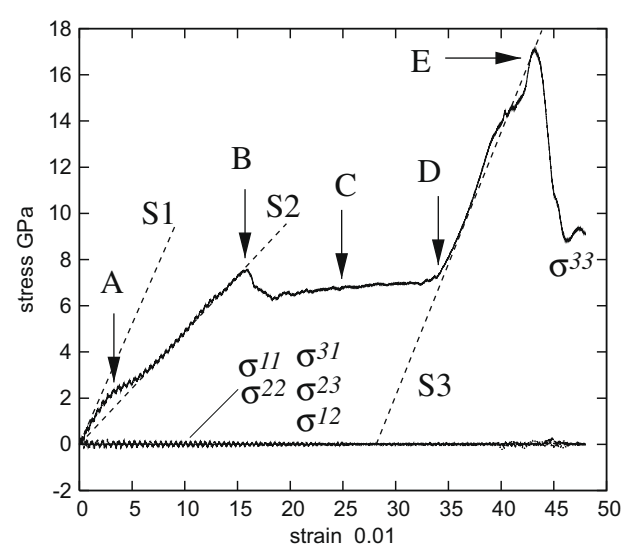

Fig. 9. Stress $\sigma^{\alpha\beta}$ and strain $\varepsilon_z(=\varepsilon^{33})$ relation obtained from FS potential.

that of loading. The results shows complete reversibility with unloading and the hysteresis is very small. The elastic curve between $\varepsilon_z = 0$–0.12 is traced back perfectly. The present EAM potential has only one minimum, the structure seems to be straightforwardly driven back to the energetic minimum point.

In the following analyses, we mainly describe the forward transformation mechanism from austenite phase to martensite one. Of course, the reverse transformation from martensite to austenite would show slight discrepancy in nucleation and propagation behaviors. However, since S–S curves for forward and reverse transformation match well, averaged behavior of reverse transformation is similar to forward one.

3.2. Evaluation of martensite detected by atomic strain measure

The atomic strain measure (ASM) corresponds to shape change between B2 and $L1_0$ structures as shown in Table 2. Therefore, it is used as a criterion for detecting MT. Fig. 11 shows distribution of ASM component ε_i^{33} of the 1D periodic model for sequential time steps in the loading simulation. With no strain, a sharp peak occurs at zero which obviously corresponds to the austenite phase (denoted by A). Then, as the external load increases, the peak emerges at greater strain (the peak moves to the right in the graph). It is found that, during transition, the peak of austenite (A) jumps to another peak which corresponds to martensite (denoted by M). The new peak (M) can be found at $\varepsilon_i^{33} > 0.10$.

As specified in Section 2.3, the transition should take place over the domain $\varepsilon_{cr}^{33} = 0.06$–$0.10$, and therefore the new peak (M) is surely owing to martensite structure. These peaks indicate that quite a few unit cell has that strain. It is guessed that the jump behavior in strain is also observed in each unit lattices. Utilizing the criterion ε_{cr}^{33}, the martensite ratio r can be defined as

$$r = \frac{\text{the number of atoms with } \varepsilon_i^{33} \geqslant \varepsilon_{cr}^{33}}{\text{total number of atoms in the specimen}}. \tag{18}$$

A middle criterion is intentionally set at $\varepsilon_{cr}^{33} = 0.05$ (called category-1, here) in case that intermediate peak appears. The final criterion is set at $\varepsilon_{cr}^{33} = 0.10$ (called category-2, here). Fig. 12 shows the time transition of r for 1D and 3D periodic models.

The results show the transition of r from 0% to 100%. In the figure, ratio of category-1 ($0.05 \leqslant \varepsilon_i^{33} < 0.10$) appears first at "FS1", but it is short-lived and vanishes at the end of the loading. On the other hand, the ratio of category-2 ($\varepsilon_i^{33} \geqslant 0.10$) begins to increase at point "FS2", and finally goes to 100%. These category-2 atoms steadily propagate during the plateau region in the S–S curve (Fig. 9). Therefore, it is judged that the martensite begins to form at "FS2". The method for detecting MT by using the ASM component works successfully with a criterion $\varepsilon_{cr}^{33} = 0.10$.

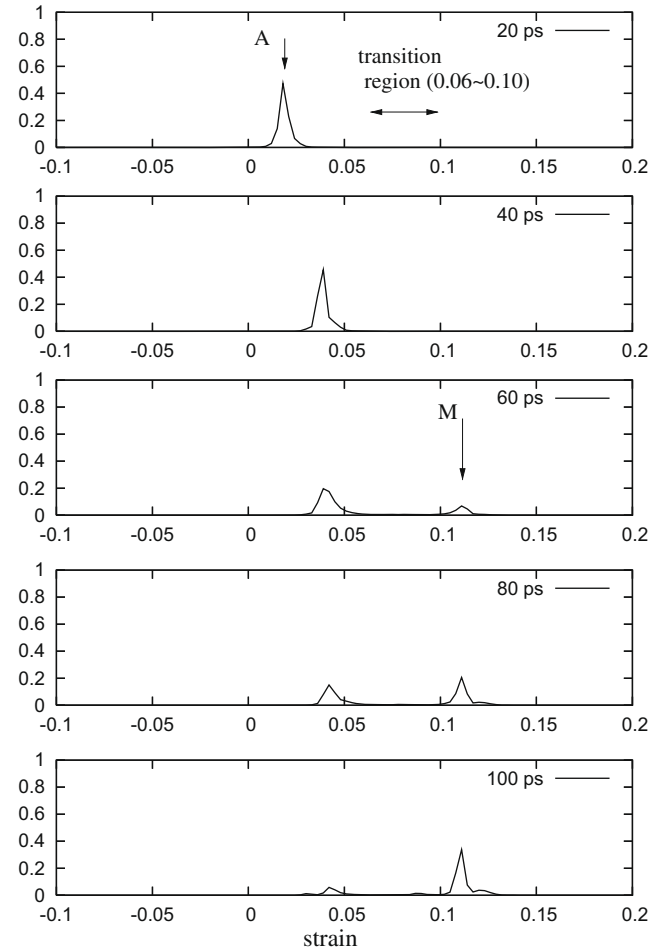

Fig. 11. Transition in population of atomic strain measure in tensile direction (ε_i^{33}). The vertical axis is the number ratio to all atoms. The peak "A" corresponds to austenite, while "M" corresponds to martensite. These two peaks are clearly separated and do not merge into each other. The interval of strain values between 0.06 and 0.10 is the domain of transition according to Table 2. Applied strain value equals 0.06, 0.12, 0.18, 0.24 or 0.30, from top to bottom.

3.3. Observation of martensite phase nucleation: Dependence on periodical condition

In the specimen surrounded by free surfaces (1D periodic model), nucleation of MT occurs at edges of the rectangular specimen. Fig. 13 shows an example of the atomic configuration viewed from

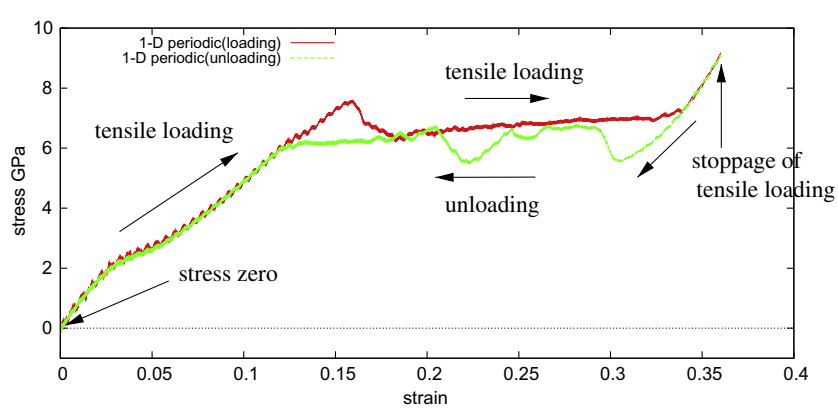

Fig. 10. Loading and unloading behavior in stress–strain ($\sigma_z - \varepsilon_z$) curve.

the edge of the specimen. Atoms with ASMs larger than the martensite criterion ($\varepsilon_{cr}^{33} = 0.10$) are rendered with relatively larger spheres. They are found around the edges. On the other hand, in the case without any surface region (3D periodic case), nucleation of MT can be observed wherever strain is likely to be localized as seen in Fig. 13c. As shown in Fig. 13b most intuitively, the case with periodic boundary condition only in one direction (2D periodic case) shows importance of the free surface for MT nucleation. Nucleation sites are observed only on the free surfaces. This picture also shows that many embryos occur almost at the same time. Thus, it is understood that MT nucleation is dominated by the strength of constraint which corresponds to the periodicity of models. In other words, there is strong surface effect on MT nucleation.

The way to transform is as follows. At the corner, two Ni atoms move apart first in the tensile direction, then the geometry of the crystal unit turns into that of martensitic structure. Nucleated martensite triggers transformation inside the specimen. Subsequently, planar interfaces between the austenite and martensite phases are formed.

The difference due to periodicity of the computation model can be found in the first yield stress and strain. Fig. 14 shows a variety of the first yield points picked up from S–S curves. The first yield behavior is assumed to be the beginning of MT. We do not mention

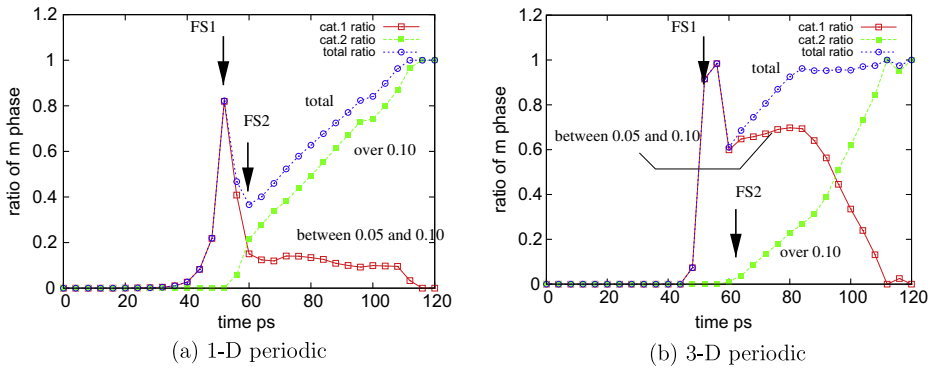

Fig. 12. Transition of martensite ratio during uniaxial tensile loading.

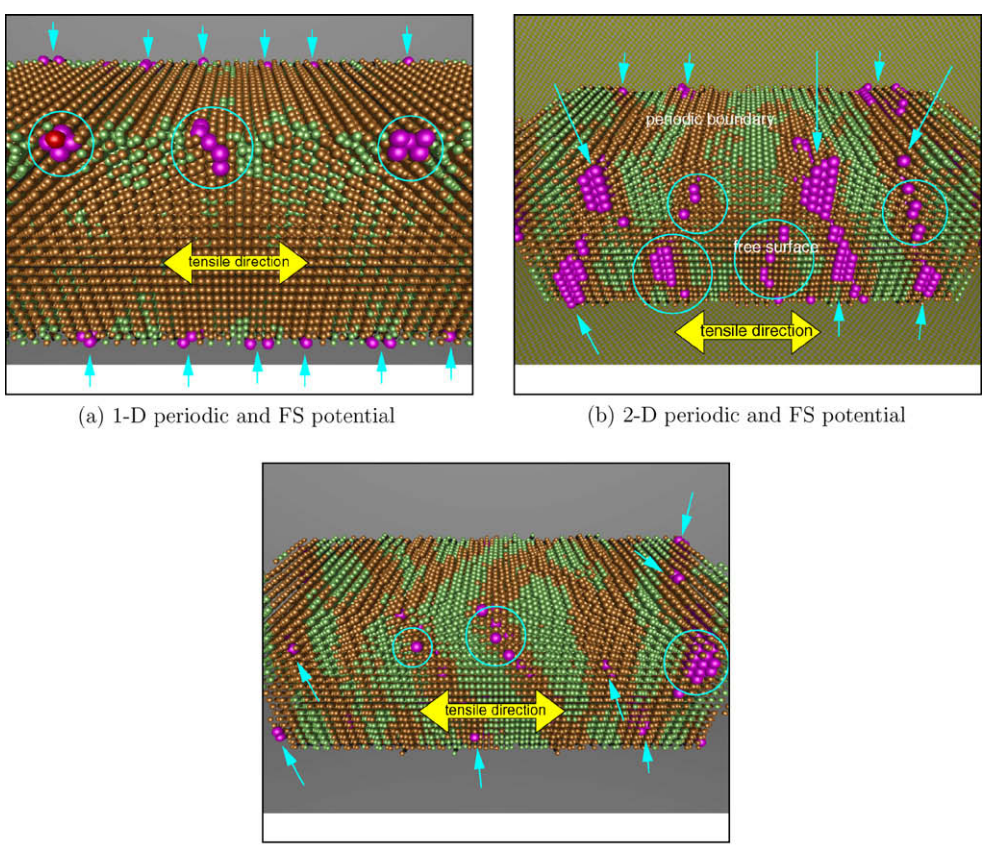

(a) 1-D periodic and FS potential

(b) 2-D periodic and FS potential

(c) 3-D periodic and FS potential

Fig. 13. Nucleation of martensite phase near surface of edges; atoms are depicted by spheres. Atoms detected as martensite are rendered with relatively larger sphere. Nucleation sites are emphasized by circles or pointed out by arrows. In the 1D periodic model they are typically found at the corner edges of the specimen, whereas in the 3D model they exist everywhere. The 2D model shows the importance of free surface most intuitively. All of the nucleation sites in 2D model are found on free surfaces.

about other specimens which have larger or smaller size, but their results are included for comparison. Generally speaking, the yielding stress and strain are greater for higher periodicity (1D < 2D < 3D). This indicates that nucleation is easy in the order: (1) corner edge (1D), (2) flat surface (1D and 2D), and (3) bulk (1D, 2D and 3D).

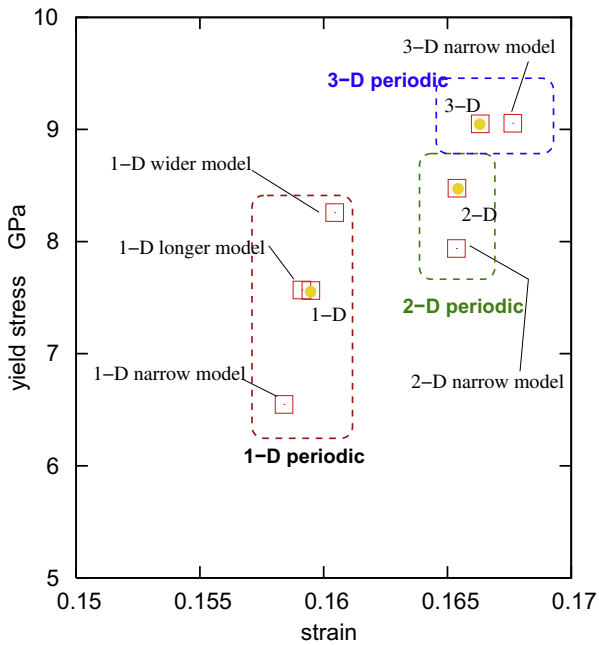

Fig. 14. Plots of the first yield point in loading simulations. Square with dot shows those for the models which are mainly discussed in the present paper. Others have different size but can be categorized with regard to periodicity, as 1D, 2D and 3D. The strain is that of the whole specimen (ε_z) and the stress is that obtained by averaging atomic stress in the tensile direction (σ_z).

3.4. Analysis of martensite phase propagation

Propagation of the martensite phase following the nucleation phenomena also varies with periodicity of the model. The transition of atomic configurations, colored by ASM value, is shown in Figs. 15 and 16. Austenite (indicated by A) and martensite (by M) are distinguished by criterion $\varepsilon_{cr}^{33} = 0.10$. Once M phase is somewhere nucleated by loading, the initial A phase steadily transforms into M phase. Especially in the 1D periodic model, which is shown in Fig. 15, clear phase fronts between M and A are observed. Curiously, phase fronts found in this simulation are remarkably similar to the experimental result of Ni–Ti material in uniaxial tension [32,33], even though the specimen is quite larger than our computational model and the elements are different from our Ni–Al. On the other hand, the 3D periodic model in Fig. 16 shows initially chaotic occurrence of M phases. But after enough strain the distributed M phases coalesce each other and finally become one large M phase.

It is found from these figures that the phase interface is inclined to the tensile direction by 45–60°. The interface plane between the initial phase (in body-centered) and product one (in face-centered) have to match between $\{110\}_{bc}$ and $\{111\}_{fc}$. These are known as "habit planes" usually discussed in MT studies. Fig. 17 explains the crystallographic relation between two habit planes. Since the ratio of lattice parameters c/a comes to around 1.32 in the unit of M phase, the habit plane $(\bar{1}11)_{fc}$ has a certain angle to (001) plane which is common to A and M phases. The angle, θ, is estimated as follows: $\theta = \tan^{-1}(c/a) \approx \tan^{-1}(1.32) = 52.9°$. On the other hand, habit plane in austenite is $(101)_{bc}$ and the angle to (001) plane is 45°. The angle of phase boundary observed in MD results comes to this range.

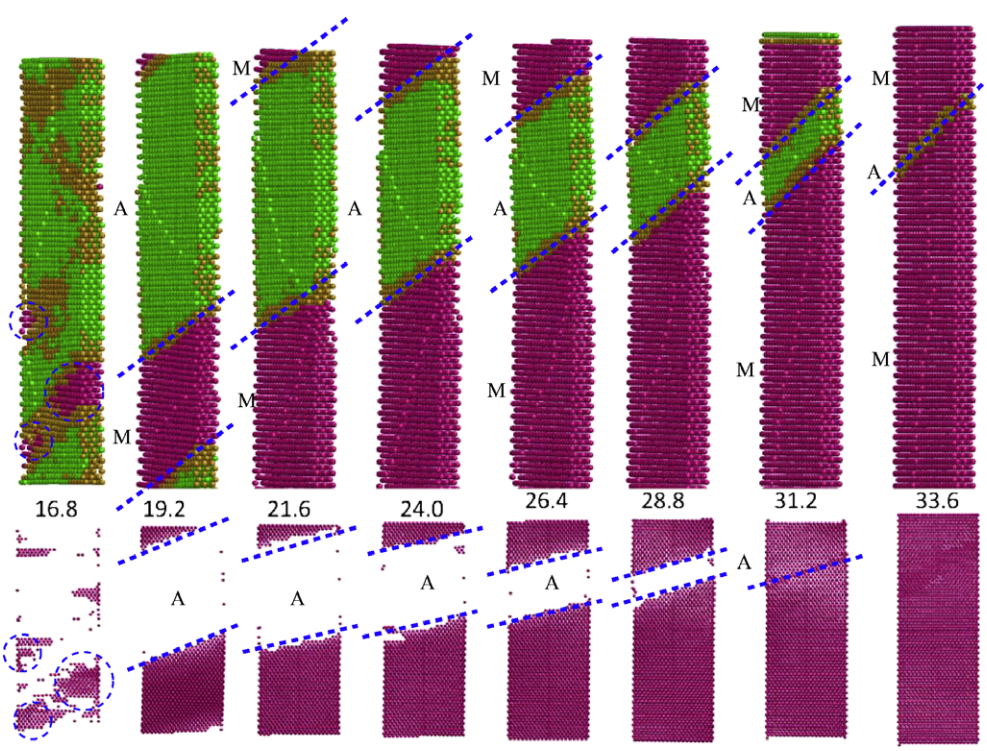

Fig. 15. Transition of phase front in the case of 1D periodic model, where A denotes austenite and M does martensite. The upper figures show only a thin slab (0.4 nm thickness) which is cut out from the specimen in parallel to the tensile direction, while the lower figures are front views of the specimen showing only martensite. The broken lines denote the obvious interfaces between austenite and martensite. The numbers in the figure denote nominal strain in percentage (e.g. "30.0" denotes $\varepsilon_z = 0.30$).

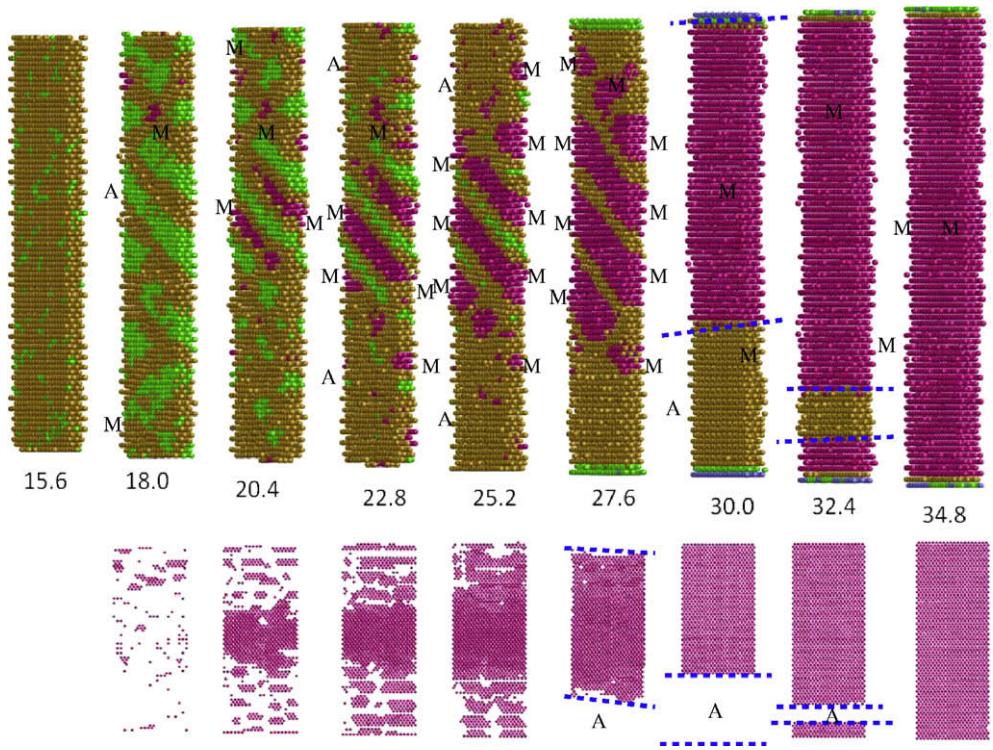

Fig. 16. Transition of phase front in the case of 3D periodic model, where "A" means austenite and "M" does martensite. The viewing method is the same as Fig. 15.

The atomic strain measure (ASM) is used to look into local distortion of crystals in the course of MD simulation. Fig. 18 shows plots of the most probable values of ASM components, ε_i^{33}, ε_i^{11}, and ε_i^{22}.

As previously mentioned, the ASM value does not show the exact value of strain. Therefore, we map ASM components to ε_1 and ε_2, which are already used as variables in the energy-deformation map (Fig. 2) and in the stress-deformation map (Fig. 4). As shown in Table 2, there are a certain relation between the ratio $c/c_0 = \varepsilon_2$ and the ASM component ε_i^{33} or between the ratio $a/a_0 = \varepsilon_1$ and the ASM component ε_i^{11}.

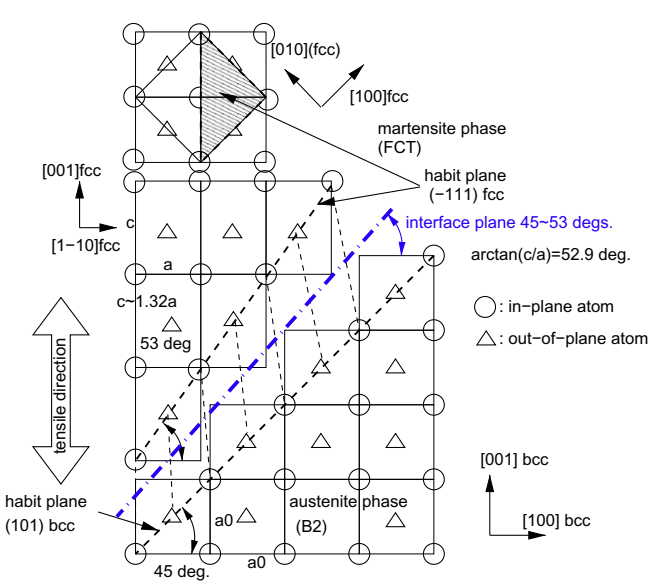

Fig. 17. Formation of interface between austenite and martensite.

What is found first is that plots are clearly discontinuous, which means that there is jump behavior in strain during the transformation event. Plots are found along the energy-minimum curve, where the stress component σ_z is not zero while both transverse stress components, σ_x and σ_y, vanish. Basically the MD results are predicted by the static energetic survey which has been done in Section 2.2.

We conclude that, in dynamics simulation of uniaxial loading, the EAM potential we use produces two distinct stable crystalline

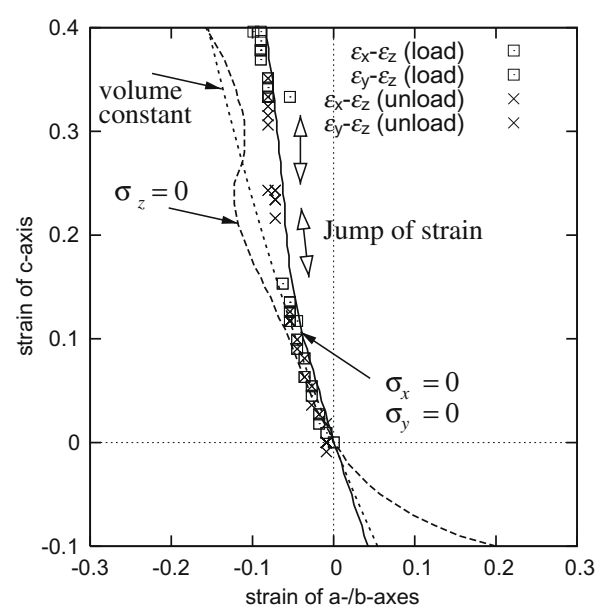

Fig. 18. Transition of atomic strain measure using peak value of 1D case. The sparsely sampled peak values which is observed in Fig.11 are mapped on $\varepsilon_1 - \varepsilon_2$ graph (axes are same as Fig. 2 or Fig.4. The austenite phase is exactly at the origin.

phases. It is not necessary to have two energy wells (minima) in potential energy map to reproduce stress-induced MT transformation. We omit discussions regarding the thermal effects on free energy. This discussion, however, is worth while doing and should be done in further study.

4. Conclusion

The basic atomistic mechanism of cubic-to-tetragonal martensitic transformation (MT) in Ni–Al alloys is studied. In order to investigate the surface effect, the straining method with variety of periodicity is added to the framework of molecular dynamics (MD). A semi-empirical potential function based on EAM framework (Finnis–Sinclair (FS) potential) which has single minimum in energy map is applicable.

1. In uniaxial loading, the FS potential produces distinct phases corresponding to austenite and martensite and shows complete recovery of shape during the unloading process. The second well in potential function is not required for obtaining martensite phase. It is found that there is jump behavior between austenite and martensite phases. The jump occurs in a plateau region which appears in stress–strain curve for the whole specimen.
2. Uniaxial condition with a variety of periodicity works well for MT simulation. The periodicity of the MD specimen raises stress and strain required for making nucleation site. When using 3D periodic cell, MT nuclei appear everywhere but they finally coalesce into one martensite.
3. The atomic strain measure (ASM), formulated using atomic coordinates, is successful in detecting the structural change of a unit crystal undergoing MT.

Acknowledgement

This work was supported by Grant in aid for abroad research (2007–2008), Kansai university and was carried out under the research program between Kansai university and Northwestern university. One of the authors (KS) greatly appreciates Northwestern university for use of computational facilities. KS also thanks C. Lee for editing.

References

[1] A. Bekker, L. Brinson, Acta Mater. 46 (1998) 3649–3665.
[2] G. Olson, Mater. Sci. Eng. A 273–275 (1999) 11–20.
[3] Q. Sun (Ed.), IUTAM Symposium on Mechanics of Martensititic Phase Transformation in Solids, Kluwer Academic Publishers, 2002.
[4] M. Daw, M. Buskes, Phys. Rev. B 29 (1984) 6443–6453.
[5] G. Olson, Mater. Sci. Eng. A. 438–440 (2006) 48–54.
[6] G. Barsch, T. Ohba, D. Hatch, Mater. Sci. Eng. A 273–275 (1999) 161–165.
[7] T. Suzuki, M. Shimono, M. Wuttig, Scripta Mater. 44 (2001) 1979–1982.
[8] P. Clapp, C. Becquart, Y. Shao, Y. Zhao, J. Rifkin, Modell. Simulat. Mater. Sci. Eng. 2 (1994) 551–558.
[9] H. Park, Nano Lett. 6–5 (2006) 958–962.
[10] R. Meyer, P. Entel, Comput. Mater. Sci. 10 (1998) 10–15.
[11] S. Ozgen, O. Adiguzel, J. Phys. Chem. Solids 65 (2004) 861–865.
[12] K. Kadau, T. Germann, P. Lomdahl, B. Holian, Science 296 (2002) 1681–1684.
[13] P. Entel, R. Meyer, K. Kadau, Philos. Mag. B 80 (2) (2000) 183–194.
[14] T. Takato, T. Uehara, Trans. Jpn. Soc. Mech. Eng. A 71 (705) (2005) 717–723.
[15] P. Clapp, M. Rubins, S. Charpenay, Z. Rifkin, J.A. Yu, A. Voter, Mater. Res. Soc. Symp. Proc. 133 (1989) 29–35.
[16] R. Kainuma, H. Nakano, K. Oikawa, K. Ishida, T. Nishizawa, Mater. Res. Soc. Symp. Proc. 246 (1992) 403–408.
[17] T. Li, J. Morris, D. Chrzan, Phys. Rev. B 70 (2004) 054107-1–054107-5.
[18] P. Potapov, P. Ochin, J. Pons, D. Schryvers, Acta Mater. 48 (2000) 3833–3845.
[19] A. Voter, S. Chen, Mater. Res. Soc. Symp. Proc. 82 (1987) 175–180.
[20] M. Yan, V. Vitek, S. Chen, Acta Mater. 44 (11) (1996) 4351–4365.
[21] S. Foiles, M. Daw, J. Mater. Res. 2 (1) (1987) 5–15.
[22] S. Rubini, P. Ballone, Phys. Rev. B 48 (1) (1993) 99–111.
[23] D. Farkas, B. Mutasa, C. Vailhe, K. Ternes, Modell. Simulat. Mater. Sci. Eng. 3 (1995) 201–214.
[24] D. Farkas, D. Roqueta, A. Vilette, K. Ternes, Modell. Simulat. Mater. Sci. Eng. 4 (1996) 359–369.
[25] M. Ludwig, P. Gumbsch, Modell. Simulat. Mater. Sci. Eng. 3 (1995) 533–542.
[26] M. Finnis, J. Sinclair, Philos. Mag. A 50 (1984) 45–55.
[27] I. Muler, A model for the simulation of shape memory behavior, in: E. Hornbogen, N. Jost (Eds.), The Martensitic Transformation in Science and Technology, Informationsgesellshaft Verlag, 1989, pp. 69–74.
[28] Y. Mishin, Interatomic potentials for metals, in: S. Yip (Ed.), Handbook of Materials Modeling, Springer, 2005, pp. 459–478.
[29] F. Milstein, J. Mater. Sci. 15 (1980) 1071–1084.
[30] P. Mott, A. Argon, U. Suter, J. Comput. Phys. 101 (1992) 140–150.
[31] M. Buehler, F. Abraham, H. Gao, Nature 426 (2003) 141–145.
[32] J. Shaw, Int. J. Plast. 16 (2000) 541–562.
[33] J. Shaw, S. Kyriakides, Int. J. Plast. 13–10 (2002) 837–871.